2020

Unveiling multiferroic proximity effect in graphene

F. Ibrahim, A. Hallal, D. S. Lerma, X. Waintal, E. Y. Tsymbal, and M. Chshiev

PAPER

Unveiling multiferroic proximity effect in graphene

2D Materials

PAPER

Unveiling multiferroic proximity effect in graphene

RECEIVED
22 August 2019

REVISED
10 October 2019

ACCEPTED FOR PUBLICATION
31 October 2019

PUBLISHED
4 December 2019

Fatima Ibrahim[1], Ali Hallal[1], Daniel Solis Lerma[1], Xavier Waintal[2], Evgeny Y Tsymbal[3] and Mairbek Chshiev[1]

[1] Univ. Grenoble Alpes, CEA, CNRS, SPINTEC, Grenoble, France
[2] Univ. Grenoble Alpes, CEA, IRIG-PHELIQS, Grenoble, France
[3] Department of Physics and Astronomy and Nebraska Center for Materials and Nanoscience, University of Nebraska, Lincoln, NE, United States of America

E-mail: fatima.ibrahim@cea.fr **and** mair.chshiev@cea.fr

Keywords: multiferroics, graphene, spintronics

Abstract

We demonstrate that electronic and magnetic properties of graphene can be tuned via proximity of multiferroic substrate. Our first-principles calculations performed both with and without spin–orbit coupling clearly show that by contacting graphene with bismuth ferrite $BiFeO_3$ (BFO) film, the spin-dependent electronic structure of graphene is strongly impacted both by the magnetic order and by electric polarization in the underlying BFO. Based on extracted Hamiltonian parameters obtained from the graphene band structure, we propose a concept of six-resistance device based on exploring multiferroic proximity effect giving rise to significant proximity electro- (PER), magneto- (PMR), and multiferroic (PMER) resistance effects. This finding paves a way towards multiferroic control of magnetic properties in two dimensional materials.

Spintronic devices possessing high speed and low-power consumption have opened new prospects for information technologies. As the spin generation, manipulation, and detection is the operating keystone of a spintronic device, realizing those three components simultaneously stands as a major challenge limiting applications [1–4]. In this context, developing a suitable spin transport channel which retains both long spin lifetime and diffusion length is highly desirable. Graphene stands as a potential spin channel material owing to its exceptional physical properties. Beside its high electron mobility and tunable-charge carrier concentration, graphene has demonstrated room temperature spin transport with long spin-diffusion lengths [5–15]. Accordingly, graphene spintronics became a promising direction of innovation that attracted a growing attention in the scientific community [16, 17].

Much efforts have been devoted to induce magnetism in graphene via different means [18–33], one of which is the exchange-proximity interaction with magnetic insulators [34–42]. Theoretically, this effect was demonstrated using different materials such as ferromagnetic [37, 38], antiferromagnetic [39], topological [40], magnetoelectric [41], or multiferroic [42] insulators where exchange-splitting band gaps reaching up to 300 meV were demonstrated. Recently, a detailed study has shown the influence of different magnetic insulators on the magnetic proximity effect induced in graphene [43]. On the other hand, experiments on YIG/Gr [34, 35, 44, 45], EuS/Gr [46], and BFO/Gr [47, 48] demonstrated proximity induced effect in graphene with substantial exchange field reaching 14 T. However, combining both conditions of a high Curie temperature (T_c) magnetic insulator and a weak graphene doping stands as a major challenge which limits practical spintronic applications.

Multiferroics, co-exhibiting a magnetic and ferroelectric order, constitute an interesting class of magnetic insulators that bring about an additional parameter in play which is the electric polarization. On one hand, proximity induced magnetism was reported in graphene using multiferroic magnetic insulator [39, 42, 49] ignoring the influence of electric polarization. On the other hand, the ferroelectrically-driven manipulation of the carrier density in graphene was demonstrated [50]. However, the ferroelectric control of magnetic proximity effect has not been addressed so far. In this letter, we report the multiferroic-induced proximity effect (MFPE) in graphene proposing the concept of controlling electronic and magnetic properties of graphene via multifferoic substrate. For this purpose, we considered bismuth ferrite $BiFeO_3$ (BFO) whose room-temperature multiferroicity promotes it

as a good candidate for applications [51–55]. Our first-principles calculations demonstrate that by contacting graphene with BFO, the spin-dependent electronic structure of graphene is highly influenced not only by the magnetic order but also by the ferroelectric polarization in the underlying BFO. These findings propose additional degrees of control for proximity induced phenomena in graphene and perhaps in other two-dimensional materials.

Our first-principles calculations are based on the projector-augmented wave (PAW) method [56] as implemented in the VASP package [57–59] using the generalized gradient approximation as parametrized by Perdew,Burke, and Ernzerhof [60, 61]. A kinetic energy cutoff of 550 eV has been used for the plane-wave basis set and a $9 \times 9 \times 1$ k-point mesh to sample the first Brillouin zone. The supercell comprises of nine (Bi–O_3–Fe) trilayers of BFO (1 1 1) surface with Fe termination sandwiched between two 4×4 graphene layers as shown in figure 1(a). We fixed the in plane lattice parameter to that of BFO where the lattice mismatch in this supercell configuration is about 1.5%. This heterostructure provides the opportunity to compare simultaneously the properties of two different graphene layers relatively sensing opposite directions of the BFO polarization P. Since maintaining the polarization is a critical issue in ferroelectric slabs, a thick BFO slab is used both to restore the electric polarization within the bulk layers and to assure that the two graphene layers do not interact. At both Gr/BFO interfaces, one Fe atom is placed at a hollow site whereas the other two atoms occupy top sites as shown in the top view of figure 1(a). Then, the atoms were allowed to relax in all directions until the forces became lower than 1 meV $\mathring{A}^{-1}$. Since we are interested in investigating the magnetic proximity effect in graphene, we have chosen this particular case of stacking with Fe surface terminations on both sides of the BFO slab so as the magnetic Fe atoms are in the vicinity of the graphene layers. This stacking is also adopted by Qiao *et al* in [39]. However, we believe that the results we are reporting on the multiferroic proximity effect in graphene will still hold qualitatively, although they might differ quantitatively, if other stacking possibilities occur. As the GGA fails to describe the electronic structure of strongly correlated oxides, we have employed the GGA+U method to the Fe-3d orbitals within the Liechtenstein 's approach [62]. We have optimized the value of U using the bulk unit cell of BFO and found that $U_{eff} = 4$ eV yields 2.44 eV band gap and $\pm 4.15\ \mu_B$/Fe magnetic moments which are in good agreement with experimental values [63–65].

Non-collinear spin ordering is an issue of particular importance in multiferroic materials. Experiments have shown that the spin cycloid in BFO thin films has a characteristic wavelength of about 64 nm which corresponds to a spin-canting angle of about 2° [66]. This canting angle is substantially small compared to that observed in other multiferroics such as $BaMnO_3$ where a 120° spin-canting angle is reported experimentally [67] and theoretically [49]. Thus, we have refrained from including non-collinear spin effects believing that such a small canting in BFO will not affect the induced proximity effect in graphene.

$BiFeO_3$ has a perovskite type cryctal structure and belongs to the polar space group $R3c$. The spontaneous polarization P along BFO (1 1 1) direction originates from the displacements of the Bi and Fe atoms from their centrosymmetric positions along the (1 1 1) direction [51, 53, 64]. To examine P of BFO after the formation of the Gr/BFO/Gr interfaces which accounts for both the ionic and charge relaxation, we show in figure 1(b) the Fe and Bi z-displacements from their centrosymmetric positions per atomic layer. It can be clearly seen that the two BFO/Gr interfaces have different values of atomic displacements whereas in the bulk layers the values are almost constant in good relevance to the bulk values (shown by dashed lines). This infers that P, which arises from such non-centrosymmetric structure, is sustained in BFO and it is perpendicular to the interface and pointing from lower graphene layer, lying at the tail of P and denoted hereafter by $Gr_{P.tail}$, towards the upper one lying at the head of P denoted by $Gr_{P.head}$. A rough estimate of the z-averaged polarization can be deduced from the values of the local polarization based on Born effective charges: $P(z) = \frac{e}{\Omega} \sum_{m=1}^{N} Z_m^* \delta z_m$; where N is the number of atoms, δz_m is the displacement of the mth atom from the centrosymmetric position, Ω is the volume of the unit cell, and Z_m^* is the Born effective charge of the mth ion. In our supercell a value of $P = 63\ \mu$C cm^{-2} is estimated which reasonably compares to the calculated value in a bulk BFO unit cell $P = 100\ \mu$C cm^{-2} [51].

We should note that in our calculations we did not apply any constraint neither on the displacement field nor on the polarization as suggested in [68, 69]. However, we performed full-ionic relaxation allowing the BFO/Gr interfaces to be formed without constraints. We believe that in our case the insulating property of the BFO slab is preserved after the formation of the Gr/BFO/Gr interfaces. As it will be shown later in the band structure plots, we can clearly notice that only graphene bands are present in the energy range in the vicinity of the Fermi-level. This means that our calculations lie in a 'nonpathologic' band alignment regime where no spill out of conduction charge into the BFO slab is occurring. In fact, the interaction at BFO/Gr interface involves both (i) the impact of graphene on the BFO surface properties and (ii) the proximity effect in graphene induced by the multiferroicity of BFO. In our current study, we focus on the latter effect only. The impact of graphene on the properties of BFO, namely magnetic properties, might be addressed later noting that such effect was reported recently in a similar interface of $BaMnO_3$/Gr [49].

We discuss now the formation of Gr/BFO/Gr interface. The BFO(1 1 1) slab is Fe^{3+} terminated on

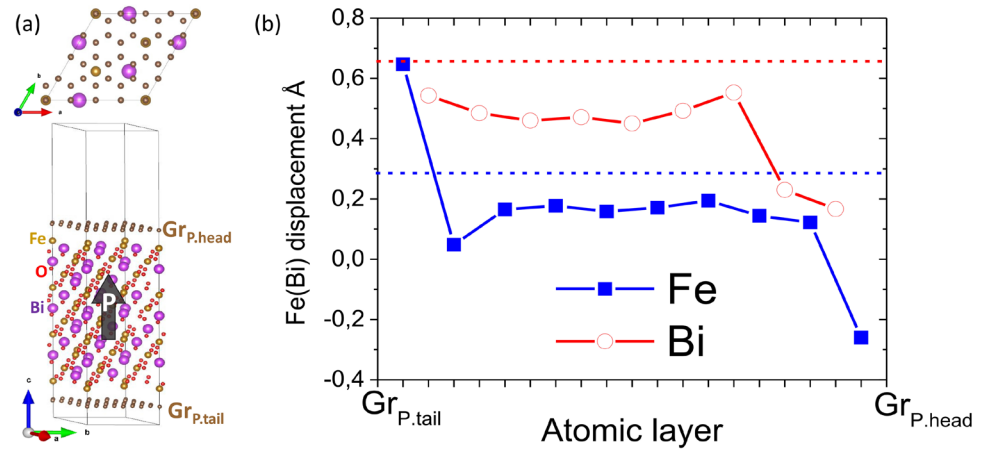

Figure 1. (a) The $Gr_{P.head}$/BFO/$Gr_{P.tail}$ supercell is shown in the lower panel. Magenta (Gold) balls designate Bi (Fe) atoms respectively and small red balls represent O atoms. A top view of the Gr/BFO interface is shown in the upper panel where one Fe atom occupies a hollow site and the other two occupy top sites. (b) The layer-by-layer Fe(Bi) displacement from their centrosymmetric positions shown by square (circle) symbols. The blue (red) dashed lines correspond to the bulk values of the displacements for Fe(Bi). The direction of the electric polarization originating from these atomic displacements is perpendicular to the interface, along the *c*-axis, and shown by an arrow.

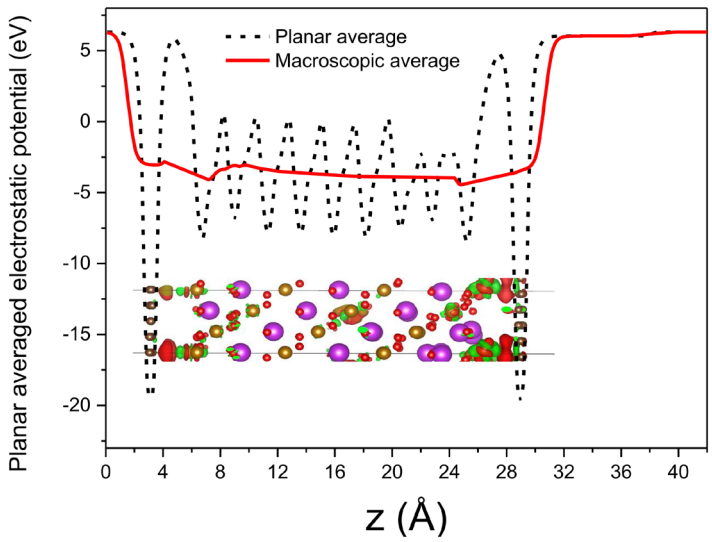

Figure 2. The calculated planar averaged electrostatic potential (dashed black line) and its macroscopic average (solid red line) across the Gr/BFO/Gr supercell. The inset shows the induced spatial charge distribution upon the formation of the two Gr/BFO interfaces. The red (green) regions indicate charge accumulation (depletion), respectively, using an isovalue $=0.002$ e Å^{-1}.

both sides which makes the two surfaces polar with a nonzero net charge. From a macroscopic electrostatic point of view, this is equivalent to a slab having a polar surface charge $\sigma_s = +1.5e/A = 88\ \mu$C cm^{-2} on both surfaces and no charges inside the slab, where A is the surface area per Fe atom. On the other hand, assuming a uniform polarization P in the BFO slab whose direction is shown in figure 1(a) yields surface polarization charges $\sigma_P = +P$ and $\sigma_P = -P$ on the *head* and *tail* surfaces, respectively. Therefore, the whole BFO slab is equivalent to a slab with total bound charge $\sigma_{head} = \sigma_s + P = 151\ \mu$C cm^{-2} on the *head* surface and $\sigma_{tail} = \sigma_s - P = 25\ \mu$C cm^{-2} on the *tail* surface. This dissimilarity in the BFO surface charges leads to the formation of two significantly different interfaces with graphene giving rise to two adsorption distances $\Delta z(\mathrm{Gr}_{P.head} - \mathrm{BFO}) = 2.35$ Å compared to $\Delta z(\mathrm{Gr}_{P.tail} - \mathrm{BFO}) = 2.7$ Å. In fact, graphene sheets adsorbed on both sides of the slab accumulate negative charges trying, ideally, to screen the positive bound charges on the BFO surfaces. This produces a strong electrostatic interaction between graphene and the BFO surfaces in particular at the *head* interface where the bound charges are quantitatively larger as shown in figure 2. Consequently, (i) the $G_{P.head}$ relaxes closer to the BFO surface compared to $G_{P.tail}$ and (ii) strong relaxations are induced at the *head* BFO surface revealed by the smaller polar displacements at the outermost layers, as shown in figure 1(b), thus, reducing the effective polarization at this surface.

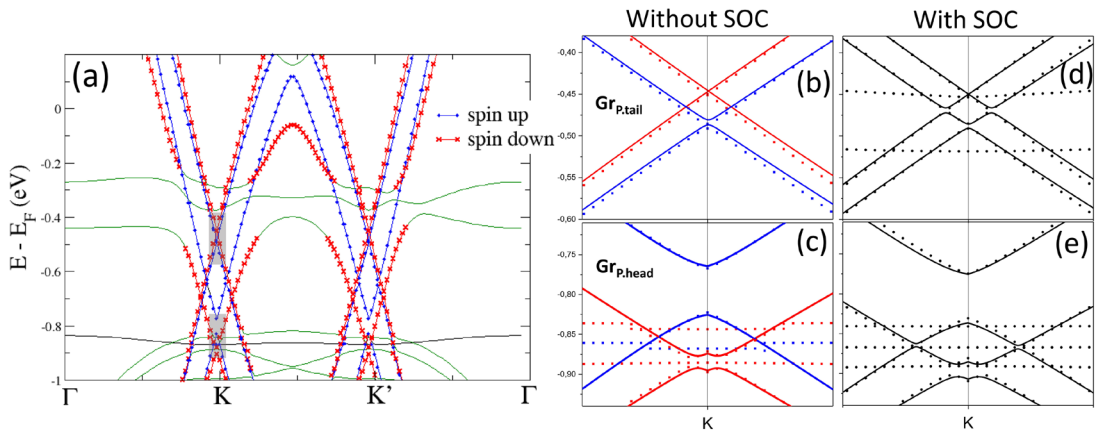

Figure 3. (a) Calculated band structure for Gr/BFO/Gr heterostructure without including spin–orbit interactions. Spin up (spin down) bands are shown in blue diamond (red cross) lines, respectively. (b), (c) are zoom around K point shown by the shaded areas in (a) corresponding to the Dirac cones for $Gr_{P.tail}$ and $Gr_{P.head}$, respectively. (d), (e) are the band structure calculated by including spin–orbit coupling shown for the same shaded region as in (b), (c) for comparison. The dotted symbols and solid lines in (b)–(e) correspond to the DFT calculated and tight-binding fitted band structures, respectively.

Table 1. Extracted energy gaps and exchange splitting parameters of $Gr_{P.head}$ and $Gr_{P.tail}$ at Dirac point for Gr/BFO/Gr heterostructure. E_G is the band-gap of the Dirac cone given in units of meV. $\Delta_\uparrow$ and $\Delta_\downarrow$ are the spin-up and spin-down gaps in meV, respectively. The spin-splitting in meV of the electron and hole bands at the Dirac cone are δ_e and δ_h, respectively. E_D in eV is the Dirac cone position with respect to Fermi level. γ_{soc} denotes the spin–orbit band opening at the avoided crossing of the spin-up and spin-down bands given in meV. The hopping parameters used to fit the tight-binding Hamiltonian to the DFT calculated band structure are denoted by $t_\uparrow$ and $t_\downarrow$ for spin up and spin down given in eV. Those are directional dependent for $Gr_{P.head}$ and their three values are listed. t_R is the strength of the Rashba spin orbit coupling given in meV.

	E_G	$\Delta_\uparrow$	$\Delta_\downarrow$	δ_e	δ_h	E_D	γ_{soc}	$t_\uparrow$	$t_\downarrow$	t_R
$Gr_{P.head}$	−48.6	55	26	104	75	−0.85	4	2.66	2.3	8.7
								2.66	2.28	
								2.61	2.32	
$Gr_{P.tail}$	−34.04	6	1.5	−35	−40	−0.47	5	2.42	2.5	7.5

To get more insights on the interaction at the Gr/BFO/Gr interfaces, the inset of figure 2 shows the induced charge distribution upon the formation of the interfaces. Negative charges, represented by red regions, are accumulated at both Gr/BFO interfaces in accord with the description we provided in the previous paragraph. However, the charges at the $Gr_{P.head}$ are obviously larger than at the $Gr_{P.tail}$. This is a direct implication of the stronger electrostatic interaction at the *head* interface which is responsible for the shorter interfacial distance.

We discuss now the induced multiferroic-proximity effect in graphene by BFO. As we have demonstrated that the two graphene sheets exhibit different interaction strengths with the underlying BFO surface, the corresponding proximity effect is expected to differ. The calculated band structure for Gr/BFO/Gr supercell, displayed in figure 3(a), reveals two distinct graphene band dispersions highlighted by blue and red corresponding to spin up and spin down, respectively. However, both graphene sheets are negatively doped, which is expected due to accumulated negative charges on graphene side in response to the positive bound charges at both BFO surfaces. Following its weaker interaction with BFO, the Dirac cone corresponding to $Gr_{P.tail}$, shown in figure 3(b) lies in the bulk gap of BFO closer to the Fermi level. On the other hand, the stronger interaction at $Gr_{P.head}$/BFO interface results in a larger doping of the Dirac point, as seen in figure 3(c). The proximity of the insulating BFO induces modifications in the linear dispersion of the graphene band structure opening a band gap at the Dirac point. This degeneracy lifting at the Dirac point is spin dependent owing to the interaction with the magnetic BFO substrate. Interestingly, the spin-dependent band gaps and exchange splittings are influenced by the interaction strength at the BFO interface. Spin dependent band-gaps are found to be 55 (26) meV for spin up (spin down) in $Gr_{P.head}$, whereas smaller values of 6 (1.5) meV are reported for $Gr_{P.tail}$. Moreover, the spin splittings for $Gr_{P.head}$ are found to be 104 (75) meV for electrons (holes), respectively, compared to 35 (40) meV for $Gr_{P.tail}$. Figures 3(d) and (e) show the evolution of the graphene band structure upon adding spin–orbit coupling to the calculations. The main impact of the spin–orbit interaction is inducing an additional band opening denoted by γ_{soc} at the spin up/spin down band crossings. We find corresponding values of 4 and 5 meV for $Gr_{P.head}$ and $Gr_{P.tail}$, respectively.

The parameters obtained from the band structure are summarized in table 1 for both $Gr_{P.head}$ and

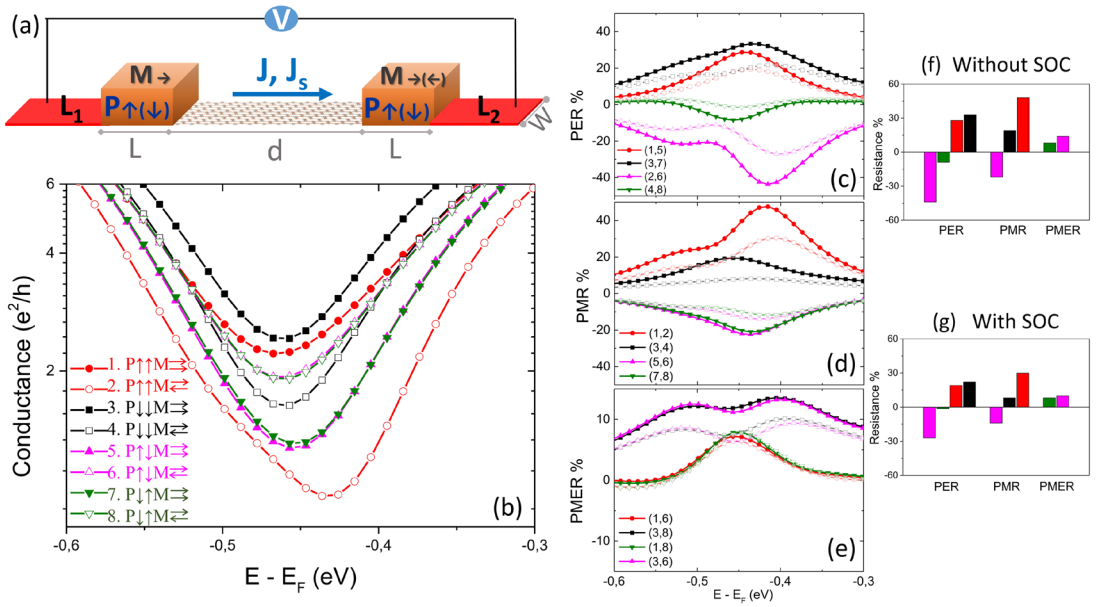

Figure 4. (a) Model spintronic device used to calculate the multiferroic proximity magnetoresistance consisting of two multiferroic regions on top of a graphene sheet. The multiferroic regions have a length L, width W and are separated by a distance d. (b) The conductances calculated without including spin–orbit coupling for the different configurations of electric polarization P and magnetization M of the two multiferroic regions. The corresponding eight conductance states are explicitly given and indexed by numbers. (c)–(e) The proximity electro (PER), magneto (PMR), and multiferroic (PMER) magnetoresistances, respectively, calculated without (closed symbols) and with (open symbols) inlcuding spin−orbit coupling. The indices of the two conductance states used to obtain each proximity resistance curve are designated. The maximum values of the PER, PMR, and PMER calculated without and with including spin−orbit coupling are shown in (f) and (g), respectively.

$Gr_{P.tail}$. E_G and $\Delta_{\uparrow(\downarrow)}$ represent the energy band gap and the spin dependent band gaps, respectively. The spin splitting of the electron and hole bands are denoted as δ_e and δ_h. E_D indicates how large the Dirac point doping is with respect to Fermi energy and γ_{soc} is the spin–orbit coupling induced band opening. The negative value of E_G indicates a spin resolved band overlap while spin splittings are defined by spin-dependent energy differences at Dirac point with negative value indicating that spin-up bands are lower in energy than that of spin-down bands. Due to the stronger interaction at the *head* interface compared to the *tail*, the proximity-induced gaps and splittings are larger in Gr_{head}. However, the spin−orbit coupling induced gap γ_{soc} is rather smaller. We should note here that our calculated values are different from those obtained in [39] due basically to the difference in the k-mesh size. As the band structure of graphene is highly sensitive to the k-mesh, we have used a dense $9 \times 9 \times 1$ k-mesh in our calculations.

The following tight-binding Hamiltonian describes the graphene's linear dispersion relation in proximity of a magnetic insulator:

$$H = \sum_{i\sigma}\sum_{l} t_{l\sigma} c^{\dagger}_{(i+l)1\sigma} c_{i0\sigma} + \text{h.c.} + \sum_{i\sigma\sigma'}\sum_{\mu=0}^{1} [\delta + (-1)^{\mu}\Delta_{\delta}]\, c^{\dagger}_{i\mu\sigma} [\vec{m}.\vec{\sigma}]_{\sigma\sigma'} c_{i\mu\sigma'} + \sum_{i\sigma}\sum_{\mu=0}^{1} [E_D + (-1)^{\mu}\Delta_s]\, c^{\dagger}_{i\mu\sigma} c_{i\mu\sigma}, \quad (1)$$

where $t_{l\sigma}$ is the anisotropic hopping connecting unit cells i to their nearest neighbors cells $i + l$. $c^{\dagger}_{i\mu\sigma}$ creates an electron of type $(\mu = 0, 1)$ corresponding to A and B sites, respectively, on the unit cell i with spin $(\sigma = 0, 1)$ for spin up and spin down electrons, respectively. $\Delta_{\delta} = \frac{\delta_e - \delta_h}{2}$ where δ_e and δ_h is the strength of the exchange spin-splitting of the electron and hole bands at the Dirac cone, respectively. $\vec{m}$ is a unit vector that points in the direction of the magnetization and $\vec{\sigma}$ is the vector of Pauli matrices, so that $\vec{m} \cdot \vec{\sigma} = m_x\sigma^x + m_y\sigma^y + m_z\sigma^z$. E_D is the Dirac position with respect to the Fermi level and $\Delta_s = \frac{\Delta_{\uparrow} + \Delta_{\downarrow}}{2}$ is the averaged staggered sublattice potential. The Rashba spin−orbit coupling term is written as [70, 71],

$$H_{SO} = it_R \sum_{i\sigma\sigma'}\sum_{l} c^{\dagger}_{(i+l)1\sigma} [\sigma^x_{\sigma\sigma'} d^x_l - \sigma^y_{\sigma\sigma'} d^y_l] c_{i0\sigma'} + \text{h.c.}, \quad (2)$$

where t_R is the Rashba spin−orbit coupling strength and the vector $\vec{d}_l = (d^x_l, d^y_l)$ connects the two nearest neighbors.

To obtain the hopping values, the tight-binding bands where fitted in good accordance to the DFT bands as shown by solid lines in figures 3(b)–(e). In the case of $Gr_{P.head}$, it was necessary to include direction dependent hopping parameters into the model. The values of the hopping parameters used for both $Gr_{P.head}$ and $Gr_{P.tail}$ are listed in table 1. We should note that using a thick BFO slab 20 Å in our DFT calculations was essential to decouple the two, $Gr_{P.head}$ and $Gr_{P.tail}$,

interfaces. Accordingly, this allows to use the DFT band structure parameters for each interface independently to further perform the tight-binding calculations.

Based on the Hamiltonian parameters extracted from the graphene band structure, we employed the tight-binding approach with scattering matrix formalism conveniently implemented within the KWANT package in order to calculate conductances and proximity resistances [72]. The system modeled is shown in figure 4(a) and comprises two identical proximity induced multiferroic regions of width $W = 39.6$ nm and length $L = 49.2$ nm, separated by a distance $d = 1.5$ nm of nonmagnetic region of graphene sheet with armchair edges. Both magnetic graphene regions are connected to the leads L_1 and L_2 and modeled using the Hamiltonian parameters. All the relative magnetization and polarization configurations are considered in this model device. The conductance in the linear response regime can be obtained according to:

$$G^{\sigma,\sigma'}_{\alpha,\alpha'} = \frac{e}{h}\sum_{\sigma}\int T^{\sigma,\sigma'}_{\alpha,\alpha'}\left(\frac{-\partial f}{\partial E}\right)dE, \qquad (3)$$

where $T^{\sigma,\sigma'}_{\alpha,\alpha'}$ indicates spin-dependent transmission probability with (α, α') and (σ, σ') being, respectively, the relative polarization and magnetization configurations in the multiferroic regions. $f = \frac{1}{e^{(E-\mu)/k_BT}+1}$ is the Fermi–Dirac distribution in which μ and T indicate electrochemical potential and temperature, respectively. It is important to mention that the temperature smearing has been taken into account using the room temperature since the Curie termperature of BFO is well above it. In order to show the impact of polarization on transport calculations, we choose to adjust the doping energy for the $Gr_{P.head}$ to be the same as for $Gr_{P.tail}$ bands. The conductance curves shown in figure 4(b), which are explicitly described in the legend and indexed by numbers, reveal six different resistance states among eight two of which are degenerate; those are (5 and 7) and (6 and 8). The conductance for a given energy should be seen as if one could gate the whole device to bring the region of interest, in the vicinity of the Dirac cone splittings, to the Fermi level. We observe that the conductance curves are splitted the most in the energy range affected by proximity effect which is around -0.47 eV. Since the gaps and exchange splittings are much larger for $Gr_{P.head}$ compared to $Gr_{P.tail}$, a difference in the energies and conductance values between the corresponding conductance states is observed.

The different combinations of these conductance states give rise to three types of proximity resistances: proximity electroresistance (PER), proximity magnetoresistance (PMR), and proximity multiferroic resistance (PMER). We introduce the generalized formulas of these three types of proximity resistances as follows:

$$\mathrm{PER}^{\sigma,\sigma'}_{\alpha} = \frac{G^{\sigma,\sigma'}_{\alpha,\alpha} - G^{\sigma,\sigma'}_{\alpha,-\alpha}}{G^{\sigma,\sigma'}_{\alpha,\alpha} + G^{\sigma,\sigma'}_{\alpha,-\alpha}} \qquad (4)$$

$$\mathrm{PMR}^{\sigma}_{\alpha,\alpha'} = \frac{G^{\sigma,\sigma}_{\alpha,\alpha'} - G^{\sigma,-\sigma}_{\alpha,\alpha'}}{G^{\sigma,\sigma}_{\alpha,\alpha'} + G^{\sigma,-\sigma}_{\alpha,\alpha'}} \qquad (5)$$

$$\mathrm{PMER}^{\sigma}_{\alpha} = \frac{G^{\sigma,\sigma}_{\alpha,\alpha} - G^{\sigma,-\sigma}_{\alpha,-\alpha}}{G^{\sigma,\sigma}_{\alpha,\alpha} + G^{\sigma,-\sigma}_{\alpha,-\alpha}}. \qquad (6)$$

Based on this formalism, sixteen different conductance states are expected. However, due to symmetry in our considered model device we obtain $G^{\sigma,-\sigma}_{\alpha,\alpha'} = G^{-\sigma,\sigma}_{\alpha,\alpha'}$ and $G^{\sigma,\sigma'}_{\alpha,-\alpha} = G^{\sigma,\sigma'}_{-\alpha,\alpha}$ and, consequently, we end up with six conductance states $G^{\sigma,\sigma'}_{\alpha,\alpha'}$.

The calculated PER, PMR, and PMER are plotted in figures 4(c)–(e), respectively, in which the indices of the two conductance states used to obtain each proximity resistance curve are designated. Closed (open) symbol lines correspond to the calculations without (with) including SOC. Owing to the two degenerate conductance states, we obtain one (two) degenerate PMR (PMER) curves, correspondingly. The PER values range between -44% and $+33\%$, PMR has values from -22% to $+48\%$, whereas PMER ranges between $+7\%$ and $+13\%$. We should note that including SOC does not change our results qualitatively but rather decreases the values of the conductances and consequently the values of the different types of proximity resistances as shown in figures 4(f) and (g). This is basically due to the mixing of the spin channels imposed by the spin–orbit interaction. Our findings lead to a concept of multi-resistance device and pave a way towards multiferroic control of magnetic properties in two-dimensional materials. Interestingly, recent experiments have demonstrated the electric control of magnetic proximity effect at the graphene/BFO interface [73] which further enhances the possibility of realizing our proposed concept device.

In conclusion, we have demonstrated that the magnetic proximity effect in graphene can be tuned by the electric polarization existing in the multiferroic substrate. The presence of electric polarization together with the polar surface charges lead to different interaction strength at the Gr/BFO interface depending on the relative direction of the electric polarization. Consequently, the spin-dependent band gaps and exchange splittings are impacted. Those findings suggest tuning the magnetic proximity effect in graphene through altering the direction or even the magnitude of the electric polarization. Such approach is accessible in multiferroic oxides where the interplay between electric and magnetic order offers the possibility of tuning the magnetization and polarization by applying electric or magnetic fields, respectively.

Acknowledgments

We thank J Fabian, K Zollner and S Roche for fruitful discussions. This project has received funding from the European Union's Horizon 2020 research and innovation programme under Grant agreements No. 696656 and 785219 (Graphene Flagship). We also acknowledge support from French ANR Project

FEOrgSPIN (ANR-18-CE24-0017). Research at University of Nebraska-Lincoln was supported by the National Science Foundation (grant ECCS-1740136) and the Semiconductor Research Corporation (nCORE program).

ORCID iDs

Mairbek Chshiev https://orcid.org/0000-0001-9232-7622

References

[1] Chappert C, Fert A and Dau F N 2007 The emergence of spin electronics in data storage *Nat. Mater.* **6** 813–23
[2] Zutić I, Fabian J and Sarma S D 2004 Spintronics: fundamentals and applications *Rev. Mod. Phys.* **76** 323
[3] Lou X, Adelmann C, Crooker S A, Garlid E S, Zhang J, Reddy K S M, Flexner S D, Palmstrøm C J and Crowell P A 2007 Electrical detection of spin transport in lateral ferromagnet-semiconductor devices *Nat. Phys.* **3** 197–202
[4] Dash S P, Sharma S, Patel R S, Jong M P D and Jansen R 2009 Electrical creation of spin polarization in silicon at room temperature *Nature* **462** 491–4
[5] Geim A K and Novoselov K S 2007 The rise of graphene *Nat. Mater.* **6** 183–91
[6] Neto A H C, Guinea F, Peres N M R, Novoselov K S and Geim A K 2009 The electronic properties of graphene *Rev. Mod. Phys.* **81** 109
[7] Tombros N, Jozsa C, Popinciuc M, Jonkman H T and van Wees B J 2007 Electronic spin transport and spin precession in single graphene layers at room temperature *Nature* **448** 571–4
[8] Popinciuc M, Józsa C, Zomer P J, Tombros N, Veligura A, Jonkman H T and van Wees B J 2009 Electronic spin transport in graphene field-effect transistors *Phys. Rev.* B **80** 214427
[9] Dlubak B, Seneor P, Anane A, Barraud C, Deranlot C, Deneuve D, Servet B, Mattana R, Petroff F and Fert A 2010 Are al_2o_3 and mgo tunnel barriers suitable for spin injection in graphene? *Appl. Phys. Lett.* **97** 092505
[10] Han W and Kawakami R K 2011 Spin relaxation in single-layer and bilayer graphene *Phys. Rev. Lett.* **107** 047207
[11] Yang T-Y *et al* 2011 Observation of long spin-relaxation times in bilayer graphene at room temperature *Phys. Rev. Lett.* **107** 047206
[12] Maassen T, van den Berg J J, IJbema N, Fromm F, Seyller T, Yakimova R and van Wees B J 2012 Long spin relaxation times in wafer scale epitaxial graphene on SiC(0 0 0 1) *Nano Lett.* **12** 1498–502
[13] Dlubak B *et al* 2012 Highly efficient spin transport in epitaxial graphene on SiC *Nat. Phys.* **8** 557–61
[14] Cummings A W and Roche S 2016 Effects of dephasing on spin lifetime in ballistic spin–orbit materials *Phys. Rev. Lett.* **116** 086602
[15] Tuan D V, Ortmann F, Cummings A W, Soriano D and Roche S 2016 Spin dynamics and relaxation in graphene dictated by electron–hole puddles *Sci. Rep.* **6** 21046
[16] Roche S *et al* 2015 Graphene spintronics: the european flagship perspective *2D Mater.* **2** 030202
[17] Han W, Kawakami R K, Gmitra M and Fabian J 2014 Graphene spintronics *Nat. Nanotechnol.* **9** 794–807
[18] Yazyev O V and Helm L 2007 Defect-induced magnetism in graphene *Phys. Rev.* B **75** 125408
[19] Yazyev O V 2008 Magnetism in disordered graphene and irradiated graphite *Phys. Rev. Lett.* **101** 037203
[20] Yazyev O V 2010 Emergence of magnetism in graphene materials and nanostructures *Rep. Prog. Phys.* **73** 056501
[21] Son Y-W, Cohen M L and Louie S G 2006 Half-metallic graphene nanoribbons *Nature* **444** 347–49
[22] Kim W Y and Kim K S 2008 Prediction of very large values of magnetoresistance in a graphene nanoribbon device *Nat. Nanotechnol.* **3** 408–12
[23] Bai J, Zhong X, Jiang S, Huang Y and Duan X 2010 Graphene nanomesh *Nat. Nanotechnol.* **5** 190–4
[24] Yang H-X, Chshiev M, Boukhvalov D W, Waintal X and Roche S 2011 Inducing and optimizing magnetism in graphene nanomeshes *Phys. Rev.* B **84** 214404
[25] Trolle M L, Møller U S and Pedersen T G 2013 Large and stable band gaps in spin-polarized graphene antidot lattices *Phys. Rev.* B **88** 195418
[26] Soriano D, Leconte N, Ordejón P, Charlier J-C, Palacios J-J and Roche S 2011 Magnetoresistance and magnetic ordering fingerprints in hydrogenated graphene *Phys. Rev. Lett.* **107** 016602
[27] McCreary K M, Swartz A G, Han W, Fabian J and Kawakami R K 2012 Magnetic moment formation in graphene detected by scattering of pure spin currents *Phys. Rev. Lett.* **109** 186604
[28] Chan K T, Neaton J B and Cohen M L 2008 First-principles study of metal adatom adsorption on graphene *Phys. Rev.* B **77** 235430
[29] Ding J, Qiao Z, Feng W, Yao Y and Niu Q 2011 Engineering quantum anomalous/valley hall states in graphene via metal-atom adsorption: an *ab initio* study *Phys. Rev.* B **84** 195444
[30] Zhang H, Lazo C, Blügel S, Heinze S and Mokrousov Y 2012 Electrically tunable quantum anomalous hall effect in graphene decorated by 5d transition-metal adatoms *Phys. Rev. Lett.* **108** 056802
[31] Jiang H, Qiao Z, Liu H, Shi J and Niu Q 2012 Stabilizing topological phases in graphene via random adsorption *Phys. Rev. Lett.* **109** 116803
[32] Kim W Y and Kim K S 2010 Tuning molecular orbitals in molecular electronics and spintronics *Acc. Chem. Res.* **43** 111–20
[33] Yang J W, Lee G, Kim J S and Kim K S 2011 Gap opening of graphene by dual fecl3-acceptor and k-donor doping *J. Phys. Chem. Lett.* **2** 2577–81
[34] Wang Z, Tang C, Sachs R, Barlas Y and Sh J 2015 Proximity-induced ferromagnetism in graphene revealed by the anomalous hall effect *Phys. Rev. Lett.* **114** 016603
[35] Leutenantsmeyer J C, Kaverzin A A, Wojtaszek M and van Wees B J 2017 Proximity induced room temperature ferromagnetism in graphene probed with spin currents *2D Mater.* **4** 014001
[36] Singh S, Katoch J, Zhu T, Meng K-Y, Liu T, Brangham J T, Yang F, Flatté M E and Kawakami R K 2017 Strong modulation of spin currents in bilayer graphene by static and fluctuating proximity exchange fields *Phys. Rev. Lett.* **118** 187201
[37] Yang H X, Hallal A, Terrade D, Waintal X, Roche S and Chshiev M 2013 Proximity effects induced in graphene by magnetic insulators: first-principles calculations on spin filtering and exchange-splitting gaps *Phys. Rev. Lett.* **110** 046603
[38] Sakai S *et al* 2016 Proximity-induced spin polarization of graphene in contact with half-metallic manganite *ACS Nano* **10** 7532–41
[39] Qiao Z, Ren W, Chen H, Bellaiche L, Zhang Z, MacDonald A and Niu Q 2014 Quantum anomalous hall effect in graphene proximity coupled to an antiferromagnetic insulator *Phys. Rev. Lett.* **112** 116404
[40] Vobornik I, Manju U, Fujii J, Borgatti F, Torelli P, Krizmancic D, Hor Y S, Cava R J and Panaccione G 2011 Magnetic proximity effect as a pathway to spintronic applications of topological insulators *Nano Lett.* **11** 4079–82
[41] Takenaka H, Sandhoefner S, Kovalev A A and Tsymbal E Y 2019 Magnetoelectric control of topological phases in graphene *Phys. Rev.* B **100** 125156
[42] Zanolli Z 2016 Graphene-multiferroic interfaces for spintronics applications *Sci. Rep.* **6** 31346

[43] Hallal A, Ibrahim F, Yang H, Roche S and Chshiev M 2017 Tailoring magnetic insulator proximity effects in graphene: first-principles calculations *2D Mater.* **4** 025074
[44] Mendes J B S, Alves Santos O, Meireles L M, Lacerda R G, Vilela-Leão L H, Machado F L A, Rodríguez-Suárez R L, Azevedo A and Rezende S M 2015 Spin-current to charge-current conversion and magnetoresistance in a hybrid structure of graphene and yttrium iron garnet *Phys. Rev. Lett.* **115** 226601
[45] Evelt M, Ochoa H, Dzyapko O, Demidov V E, Yurgens A, Sun J, Tserkovnyak Y, Bessonov V, Rinkevich A B and Demokritov S O 2017 Chiral charge pumping in graphene deposited on a magnetic insulator *Phys. Rev.* B **95** 024408
[46] Wei P *et al* 2016 Strong interfacial exchange field in the graphene/eus heterostructure *Nat. Mater.* **15** 711–6
[47] Wu Y-F *et al* 2017 Magnetic proximity effect in graphene coupled to a bifeo$_3$ nanoplate *Phys. Rev.* B **95** 195426
[48] Song H-D *et al* 2018 Asymmetric modulation on exchange field in a graphene/bifeo$_3$ heterostructure by external magnetic field *Nano Lett.* **18** 2435–41
[49] Zanolli Z, Niu C, Bihlmayer G, Mokrousov Y, Mavropoulos P, Verstraete M J and Blügel S 2018 Hybrid quantum anomalous hall effect at graphene-oxide interfaces *Phys. Rev.* B **98** 155404
[50] Baeumer C, Saldana-Greco D, Martirez J M P, Rappe A M, Shim M and Martin L W 2015 Ferroelectrically driven spatial carrier density modulation in graphene *Nat. Commun.* **6** 6371
[51] Neaton J B, Ederer C, Waghmare U V, Spaldin N A and Rabe K M 2005 First-principles study of spontaneous polarization in multiferroic $BiFeO_3$ *Phys. Rev.* B **71** 014113
[52] Ravindran P, Vidya R, Kjekshus A, Fjellvåg H and Eriksson O 2006 Theoretical investigation of magnetoelectric behavior in $BiFeO_3$ *Phys. Rev.* B **74** 224412
[53] Wang J *et al* 2003 Epitaxial $BiFeO_3$ multiferroic thin film heterostructures *Science* **299** 1719–22
[54] Zavaliche F, Yang S Y, Zhao T, Chu Y H, Cruz M P, Eom C B and Ramesh R 2006 Multiferroic $BiFeO_3$ films: domain structure and polarization dynamics *Phase Transit.* **79** 991–1017
[55] Béa H *et al* 2009 Evidence for room-temperature multiferroicity in a compound with a giant axial ratio *Phys. Rev. Lett.* **102** 217603
[56] Blöchl P E 1994 Projector augmented-wave method *Phys. Rev.* B **50** 17953–79
[57] Kresse G and Hafner J 1993 *Ab initio* molecular dynamics for liquid metals *Phys. Rev.* B **47** 558–61
[58] Kresse G and Furthmüller J 1996 Efficient iterative schemes for *ab initio* total-energy calculations using a plane-wave basis set *Phys. Rev.* B **54** 11169–86
[59] Kresse G and Furthmüller J 1996 Efficiency of *ab initio* total energy calculations for metals and semiconductors using a plane-wave basis set *Comput. Mater. Sci.* **6** 15–50
[60] Perdew J P, Burke K and Ernzerhof M 1996 Generalized gradient approximation made simple *Phys. Rev. Lett.* **77** 3865–8
[61] Kresse G and Joubert D 1999 From ultrasoft pseudopotentials to the projector augmented-wave method *Phys. Rev.* B **59** 1758–75
[62] Liechtenstein A I, Anisimov V I and Zaane J 1995 Density-functional theory and strong interactions: Orbital ordering in mott-hubbard insulators *Phys. Rev.* B **52** 5467R
[63] Sosnowska I, Schäfer W, Kockelmann W, Andersen K and Troyanchuk I 2002 Crystal structure and spiral magnetic ordering of $BiFeO_3$ doped with manganese *Appl. Phys.* A **74** s1040–2
[64] Kubel F and Schmid H 1990 Structure of a ferroelectric and ferroelastic monodomain crystal of the perovskite $BiFeO_3$ *Acta Crystallogr.* B **46** 698–702
[65] Ihlefeld J F *et al* 2008 Optical band gap of $BiFeO_3$ grown by molecular-beam epitaxy *Appl. Phys. Lett.* **92** 142908
[66] Gross I *et al* 2017 Real-space imaging of non-collinear antiferromagnetic order with a single-spin magnetometer *Nature* **549** 252–6
[67] Cussen E J and Battle P D 2000 Crystal and magnetic structures of 2H BaMnO3 *Chem. Mater.* **12** 831–8
[68] Stengel M, Spaldin N A and Vanderbilt D 2009 Electric displacement as the fundamental variable in electronic-structure calculations *Nat. Phys.* **5** 304–8
[69] Stengel M, Aguado-Puente P, Spaldin N A and Junquera J 2011 Band alignment at metal/ferroelectric interfaces: insights and artifacts from first principles *Phys. Rev.* B **83** 235112
[70] Kane C L and Mele E J 2005 Quantum spin hall effect in graphene *Phys. Rev. Lett.* **95** 226801
[71] Tse W-K, Qiao Z, Yao Y, MacDonald A H and Niu Q 2011 Quantum anomalous hall effect in single-layer and bilayer graphene *Phys. Rev.* B **83** 155447
[72] Groth C W, Wimmer M, Akhmerov A R and Waintal X 2014 Kwant: a software package for quantum transport *New J. Phys.* **16** 063065
[73] Song H-D, Zhu P-F, Yang X, Qin M, Ren Z, Duan C-G, Han G, Liao Z-M and Yu D 2018 Electrical control of magnetic proximity effect in a graphene/multiferroic heterostructure *Appl. Phys. Lett.* **113** 183101